RSC Advances

PAPER

View Article Online
View Journal | View Issue

Check for updates

Cite this: *RSC Adv.*, 2023, **13**, 35145

Physical, optoelectronic and thermoelectric characteristics of double perovskite (Sr_2ScBiO_6) for green energy technology using *ab initio* computations

Sushil Kumar Singh,[a] Jisha Annie Abraham,[b] Ayman S. Alofi,[c] Anshuman Srivastava,*[ad] K. L. Meena,[a] B. Alshahrani,[e] Ramesh Sharma *[f] and A. J. A. Moayad*[g]

This work presents the investigation of physical characteristics including structural, electronic, elastic, optical and thermoelectric, of the double perovskite (DP) oxide Sr_2ScBiO_6 with the aid of the FP-LAPW method, dependent on DFT combined with BoltzTraP code. To incorporate the inclusion of exchange as well as correlation effects, approximations like LDA and three different forms of GGA [PBE-GGA, WC-GGA & PBEsol-GGA] are applied. The mBJ-GGA method including spin-orbital coupling (SOC) & not including SOC was utilised in this investigation and it was carried out in the WIEN2k code. In addition, the TB-mBJ exchange potential analysis classified Sr_2ScBiO_6 as having a p-type semiconducting nature with an indirect bandgap value of 3.327 eV. Additionally, the mechanical properties analysis and the related elastic constants demonstrate the anisotropic nature of Sr_2ScBiO_6 with decent mechanical stability. Apart from that, the Sr_2ScBiO_6 was considered a brittle non-central force solid with dominant covalent bonding. The varying optical parameter evaluations highlighted the potential use of Sr_2ScBiO_6 in visible-light (vis) and ultraviolet (UV)-based optoelectronic devices. Moreover, the semiconducting nature of Sr_2ScBiO_6 was verified through its thermoelectric response, which revealed that the charge carriers mostly consist of holes. Over a wide temperature range (100–1200 K), several transport metrics like the Seebeck coefficient (S), electrical conductivity (σ/τ), thermal conductivity (κ/τ), and power factor (PF) are investigated. An optimal value of figure of merit (ZT) ~ 0.62 at T = 1200 K is accomplished. The extremely lower value of thermal conductivity as well as higher electrical conductivity leads to a higher figure of merit of the investigated system. The Sr_2ScBiO_6 verified a high ZT value, confirming that the material would be beneficial in renewable energy and thermoelectric (TE) applications.

Received 9th August 2023
Accepted 8th November 2023

DOI: 10.1039/d3ra05397k

rsc.li/rsc-advances

1. Introduction

The pursuit of renewable energy and the growth of related technologies in the modern world has sparked significant and comprehensive research efforts that have produced many sorts of energy conversion systems. Thermoelectric materials that can transform surplus heat into electrical energy have emerged as important possibilities to address the issue of the energy crisis.[1–5] ZT is used to evaluate the thermoelectric material's performance coefficient formulated by the following equation:[6]

$$ZT = \frac{\sigma S^2 T}{\kappa} \tag{1}$$

where σ denotes electrical conductivity, S represents Seebeck coefficient, T denotes temperature and κ denotes total thermal conductivity, respectively. A substantial power factor ($S^2\sigma$) and a low heat conductivity are vital for improved thermoelectric performance. Double perovskites have been developed in the arena of thermoelectricity because of their noteworthy characteristics like tensile strength, thermal endurance, affordability, non-toxicity *etc.* The perovskite class of materials, which is made up of different mineral compounds, have gained a lot of interest from the scientific community in recent years. They have been used in a variety of trailblazing fields, like solid-oxide electrolyte fuel cells, spintronics, and perovskite based solar cells. Interestingly, due to their remarkable features that are

---

[a] *Department of Mechanical Engineering, Nirwan University, Jaipur, India. E-mail: anshuman0203@gmail.com*
[b] *Department of Physics, National Defence Academy, Pune, Maharashtra, India*
[c] *Physics Department, College of Science, Taibah University, Medina, Saudi Arabia*
[d] *Department of Mechanical Engineering, Shambhunath Institute of Engineering and Technology, Prayagraj, India*
[e] *Department of Physics, Faculty of Science, King Khalid University, P. O. Box 9004, Abha, Saudi Arabia*
[f] *Department of Applied Science, Feroze Gandhi Institute of Engineering and Technology, Raebareli 229001, Uttar Pradesh, India. E-mail: sharmadft@gmail.com*
[g] *Department of Materials Science, Malawi University of Science and Technology, P. O. Box 5196, Limbe, Malawi. E-mail: mailme_moya123@rediffmail.com*

appropriate for a widespread array of industrial fields, DPs have demonstrated a key role ahead of other materials. In fact, they have been extensively employed in multiple fields, such as heterogeneous catalysts, thermoelectricity, transparent conductors, solar energy conversion, pigments, and photocatalysts.[1–7] More recently, greater attention has been focused on the development of DPs, particularly in the development of high-temperature thermoelectric devices.[8–10] This corresponds to the rising demand for thermoelectric materials to minimise the over-reliance on the rapidly-depleting fossil fuel sources. Realising the exceptional performance of perovskite materials in thermoelectric applications, they have attracted global attention over their ability to transform waste heat into sound energy, which positions them as one of the promising open sources of green energy technologies.[11–14] One of the instruments used to assess the thermoelectric, optical, and electronic attributes of DP oxides is the Density Functional Theory (DFT). In one study, Aziz *et al.*[15] estimated the properties of X_2NaIO_6 (X = Pb, Sr) and revealed that both Sr_2NaIO_6 and Pb_2NaIO_6 exhibited good semiconducting behaviours with direct bandgaps (E_g) of 5.48 and 3.75 eV, respectively. In addition, Sr_2NaIO_6 achieved a higher *ZT* value and Power Factor (PF) of 0.7728 and 206.3, respectively. In addition, the cubic X_2NaIO_6 (X = Pb, Sr) was more suitable in thermoelectric (TE) applications and optoelectronic devices.[15] In another study, Parrey *et al.*[16] assessed the La_2NbMnO_6 DP. Based on the findings, La_2NbMnO_6 was suggested as having a half-metallic nature with an E_g of 3.75 eV. Moreover, the significant absorption of the entire infrared (IR) and ultraviolet (UV) spectra by La_2NbMnO_6 implies its potential application in UV and IR-based optoelectronic devices.[16] Furthermore, Rameshe *et al.*[17] examined the physical properties of Sr_2AlNbO_6 and Sr_2AlTaO_6 in cubic symmetry. Several optical properties were calculated. Besides, the electronic structure was applied to determine the different Seebeck coefficients under various temperature conditions at varying carrier concentrations. According to the findings, the existence of bandgap in both compounds indicates that both Sr_2AlNbO_6 and Sr_2AlTaO_6 were semiconducting materials.[17] Meanwhile, Dar *et al.*[18] reported that the semiconducting nature of Ba_2InTaO_6 was verified by the Seebeck coefficient (S) and its electrical conductivity (σ/τ), with electrons functioning as the main carriers. Thus, the study considered that the excellent PF of Ba_2InTaO_6 would be beneficial in thermoelectric devices.[18] Additionally, AlQaisi *et al.*[19,20] evaluated the thermoelectric properties of Ba_2NaIO_6 and Ba_2YBiO_6. The findings demonstrated that the Ba_2NaIO_6 and Ba_2YbiO_6 compounds were p-type semiconductors with direct and indirect bandgaps, respectively. The results also highlighted the potential of both compounds as base materials in thermoelectric and optoelectronic applications.[19,20] Apart from that, Khandy *et al.*[21] analysed the physical characteristics of Ba_2CdReO_6. The study found that the compound displayed a minimal stability energy curve in the ferromagnetic (FM) setup, while the half-metallic feature was observed in the band structure. Moreover, the physical attributes of the material were the major advantages that allowed it to be widely utilised as an electrode material in spintronics applications.[21] In other studies, Hanif *et al.*[22] explored the promising characteristics of Sr_2XNbO_6 (X = La, Lu) that could be implemented in the UV region of TE and optoelectronic devices. Both Sr_2LaNbO_6 and Sr_2LuNbO_6 exhibited direct bandgaps of 4.02 and 3.7 eV, respectively. Also, Haid *et al.* inspected the optical properties of Sr_2CrTaO_6 and demonstrated the suitability of the compound in a broad range of visible light (vis), UV, and IR-based applications. The Sr_2CrTaO_6 also exhibited a half-metallic ferrimagnetic ground state.[28] Abraham *et al.* studied the structural, electronic, optical, thermoelectric, and SLME properties of DP oxide Pb_2ScBiO_6.[29] Recently, Manzoor *et al.* computed the structural, electronic, electron localization function (ELF), mechanical, optical, and thermoelectric, properties of Sr_2BTaO_6 (B = Sb, Bi) DP oxides using the *ab initio* method.[30] Based on the above literature, Sr_2ScBiO_6 is one of the promising members of the perovskite family that has not been fully explored in terms of its thermoelectric, electronic, structural, and optical attributes. Previously, Kazin *et al.* evaluated the production and crystalline structure of Sr_2ScBiO_6. High-resolution electron microscopy, X-ray diffraction (XRD), and electron diffraction were utilised to analyse the crystal structure. Based on the results, the Sr_2ScBiO_6 was synthesised *via* a solid-state reaction technique in which the substance acquired the coveted oxygen stoichiometry at 850 °C and remained stable up to 1150 °C. Regarding the structural features, Sr_2ScBiO_6 demonstrated a perovskite-derived rock-salt ordering of Bi^{5+} and Sc^{3+} on the B locations. In addition, the tolerance factor of the Sr_2ScBiO_6 was estimated to be 0.93.[31] In another study, Sr_2ScBiO_6 was prepared using oxides and carbonates through the nitrate route and compressed into a pellet. Subsequently, the pellet was burnt in a tubular furnace at 1050 °C for 72 h. The XRD analysis showed that the Sr_2ScBiO_6 was phase-pure and exhibited a face-centred cubic (FCC) phase holding lattice parameter of 8.192 Å.[32] Even though the published studies on this Sr_2ScBiO_6, adequate investigation into Sr_2ScBiO_6 using the most prominent DFT techniques is lacking.[33] Meanwhile, the overwhelming demand for raw materials to satisfy the growing worldwide industrialisation has outlined the urgent need to minimise global energy usage and explore alternative renewable energy sources. Concurrently, recent advance in quantum modelling and computing power has enabled researchers to perform accurate and efficient quantum mechanical calculations. This, in turn, provides the opportunity to extrapolate the calculating power such that even the previously complex properties of certain materials could now be identified and measured with pinpoint accuracy.[34] Therefore, this study aimed to perform an *ab initio* investigation of double perovskite Sr_2ScBiO_6 as a suitable low-cost material for green energy applications using the DFT approach. This work involved the use of the LDA,[35] PBE-Generalised Gradient Approximation (GGA),[36] WC-GGA,[37] PBEsol[38] and modified Becke–Johnson (mBJ) potential methods[39] to recognize the thermoelectric, electronic, optical, and structural attributes of Sr_2ScBiO_6. Additionally, the BoltzTrap code[40] was utilised to determine the thermoelectric properties of the compound. It is expected that the present research will establish critical insights for future experimental and theoretical research.

2. Computational method

This study employed the first-principles-dependent FP-LAPW scheme for the computation process following the WIEN2k package,[41] which is the ideal approach to determine the electronic features of solids. The local density approximation (LDA),[35] Perdew–Burke–Ernzerhof (PBE) GGA version (PBE-GGA),[36] Wu–Cohen WC-GGA,[37] and PBEsol-GGA[38] methods were applied during the structural and elastic parameter calculations of the Sr_2ScBiO_6 used by PBE-GGA. Nevertheless, the PBE-GGA could only provide a precise measurement of the ground state under the energy bandgap values and structural properties of semiconductors. Therefore, the Tran–Blaha modified Becke–Johnson exchanges potential approximation (TB-mBJ)[39] was performed to accurately project the material band structure. Due to the structure containing a heavy element (Bi), the SOC interaction was applied to mBJ-GGA. In the calculation, the muffin sphere radius (R_{MT}) as well as plane-wave cut-off (K_{max}) was set to 7, while the Gaussian factor (G_{max}) was held at 12. A mesh of 14 × 14 × 14 was also applied to compute the opto-electronic evaluations, respectively. At 10^{-5} Ry, the convergence condition level was then met self-consistently. Afterwards, the R_{MT} values for the Sr, Sc, Bi, and O atoms were applied at 2.50, 2.09, 2.10, and 1.72 a.u., respectively. Expansion in the spherical harmonics inside the muffin-tin spheres was made up to the $l_{max} = 10$, while Fourier expansion charge density was set to $G_{max} = 12$ (a.u.)$^{-1}$. Elastic constants and other parameters are utilised in the IRelast suite[42] established by Murtaza for the computation of elastic properties. At last, the Boltzmann transport equation was utilised to estimate the thermoelectric features of Sr_2ScBiO_6 following the semi-classical Boltzmann transport model, as applied in the BoltzTraP[40] within the constant relaxation time approximation. The lattice thermal conductivity (κ_l) was calculated using Slack's equation. As *k*-point sampling is dependent on thermoelectric characteristics. In order to calculate the same, we have taken into account a higher dense *k*-points of 100 000.

3. Results and discussion

3.1 Structural properties

The cubic phase of the studied double perovskite oxide Sr_2ScBiO_6 has depicted in Fig. 1. The basic cubic structure of this compound has a space group of $Fm\bar{3}m$ (225). This perovskite is a grid of sharing of the corner of octahedra with monovalent Sr positioned at the centre of the octahedral cavity. Each Sr atom is bounded by 12 O atoms, while each Sc and Bi atom is surrounded by 6 O atoms. Similarly, it is perceptible from Fig. 1(a) and (b) that ScO_6 and BiO_6 octahedra are alternatively aligned in the direction of [1 0 0], [0 1 0] and [0 0 1]. The centre of each octahedron is alternatively engaged by Sc and Bi in the NaCl structure. Sr, Bi, Sc and O occupies the positions of (0.25, 0.25, 0.25), (0, 0, 0), (0.5, 0.5, 0.5), and (0.2442, 0, 0) Wyckoff sites respectively. The experimental lattice constant was applied to determine the structural characteristics of Sr_2ScBiO_6, while the total energy of the crystal structure was reduced *via* Birch–Murnaghan's equation of states *versus* the unit cell volume[43] and presented in Fig. 2.

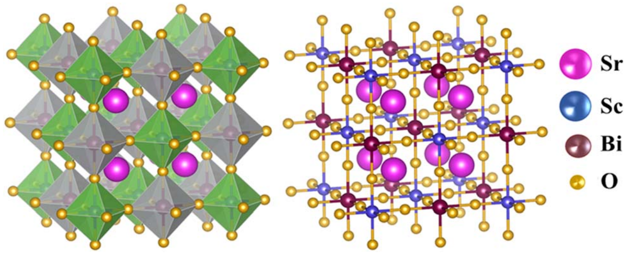

Fig. 1 Crystal structure (polyhedral and ball-and-stick) of Sr_2ScBiO_6.

$$E(V) = E_0 + \frac{9V_0B}{16}\left[\left\{\left(\frac{V_0}{V}\right)^{2/3} - 1\right\}^2 B' + \left\{\left(\frac{V_0}{V}\right)^{2/3} - 1\right\}^2 \left\{6 - 4\left(\frac{V_0}{V}\right)^{2/3}\right\}\right] \quad (2)$$

where E_0 denotes the equilibrium total energy, V_0 – equilibrium volume, V – distorted volume, B and B' – bulk modulus and its pressure derivative.

Table 1 recapitulates the computed lattice constants and other characteristics for the Sr_2ScBiO_6 using different exchange–correlation approximations (LDA, PBE-GGA, WC-GGA, PBE-sol GGA). An evaluation with earlier available theoretical as well as experimental information is also tabulated in Table 1. The predicted lattice constants of Sr_2ScBiO_6 computed by different GGA approximations are found to be higher than the experimental lattice parameters, whereas LDA generally underestimates the lattice parameters. Table 1 presents the obtained ground structure according to several lattice parameters, like lattice constant (a), bulk modulus (B), and its pressure derivative (B'), as well as the lengths of the bonds between Sr–Bi, Bi–O, Sc–O, and Sr–O. Sr_2ScBiO_6 was crystallised with space group $Fm\bar{3}m$ in an ideal cubic structure with an experimental lattice constant value of 8.1895 Å.[31,32] Interestingly, the optimised lattice constant (a) and bond lengths were close to the available experimental data,[31,32] verifying the accuracy of the present computations.

To inspect the stability of Sr_2ScBiO_6 thermodynamically, we have evaluated formation energy (H_f) and cohesive energy (E_c) using the following relations

$$H_f^{Sr_2ScBiO_6} = E_{tot}^{Sr_2ScBiO_6} - \left(2E_{Sr}^{bulk} + E_{Sc}^{bulk} + E_{Bi}^{bulk} + 6E_0^{bulk}\right) \quad (3)$$

$$E_C^{Sr_2ScBiO_6} = 2E_{Sr}^{bulk} + E_{Sc}^{bulk} + E_{Bi}^{bulk} + 6E_0^{bulk} - E_{tot}^{Sr_2ScBiO_6} \quad (4)$$

where, E_{total}, E_O, E_{Sc}, E_{Bi}, and E_{Sr} are the total energy corresponding to Sr_2ScBiO_6, O, Sc, Bi and Sr, respectively. The obtained negative H_f and positive value of E_c as tabulated in Table 1, confirm the thermodynamic stability of the studied system.[29–31] To explore the cubic phase stability of Sr_2ScBiO_6, we have used the following formulae to calculate the octahedral factor (μ) as well as the tolerance factor (τ).

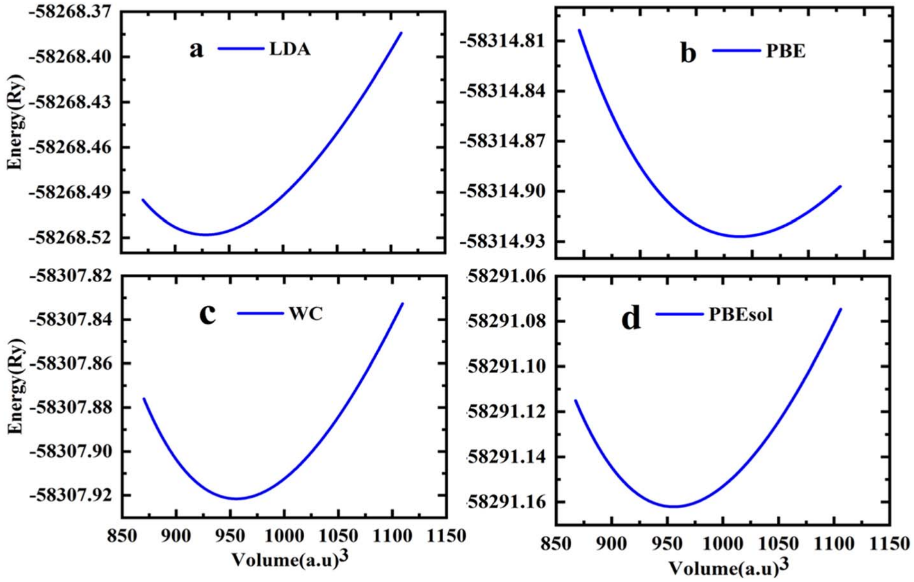

Fig. 2 Variation of total energy *versus* volume of Sr_2ScBiO_6 by (a) LDA (b) PBE-GGA (c) WC-GGA (d) PBEsol.

$$\mu = R_B/R_x \tag{5}$$

$$t = \frac{R_{Sr} + R_O}{\sqrt{2}\left(\frac{R_{Sc} + R_{Bi}}{2} + R_O\right)} \tag{6}$$

Here R_{Sr}, R_{Sc}, R_{Bi} and R_O denotes radious of the constituent atoms of Sr_2ScBiO_6. The value of tolerance factor τ must lie between 0.9 and 1.02 for a stable perovskite compound.[44] Fortuitously, the investigated double perovskite oxide has tolerance factor within the acceptable range. As can be seen from Table 1, the tolerance factor for Sr_2ScBiO_6 is found to be values 0.92 within the previously specified range, indicating that its stability in cubic structure.

3.2 Mechanical properties

The elastic coefficients were calculated to determine the mechanical performance of the Sr_2ScBiO_6. Since it was revealed that the Sr_2ScBiO_6 exhibited a cubic crystalline structure, only the elastic parameters (C_{11}, C_{12}, and C_{44}) were imperative for the mechanical characteristics analysis. As summarised in Table 2, the elastic constants of the Sr_2ScBiO_6 in this study obeyed the stability conditions including the "$C_{11} - C_{12} > 0$, $C_{11} > 0$, $C_{44} > 0$, $C_{11} + 2C_{12} > 0$". The second-order elastic constants were used to derive other elastic parameters, including bulk (B), shear (G) and Young (Y) moduli, Poisson's ratio (σ), as well as anisotropy factor (A), according to these expressions:

$$B = \frac{1}{3}(C_{11} + 2C_{12}) \tag{7}$$

$$Y = \frac{9BG}{3B + G} \tag{8}$$

$$\sigma = \frac{3B - 2G}{2(3B + G)} \tag{9}$$

$$A = \frac{2C_{44}}{C_{11} - C_{12}} \tag{10}$$

where the shear modulus (G) refers to the compound's retort to the shear deformation. The larger bulk modulus implies the remarkable forte of the Sr_2ScBiO_6 when subjected to external pressure. In addition, the low G of 89.53 GPa suggests a relatively smaller plastic twist in Sr_2ScBiO_6. Moreover, Young modulus (Y) refers to the stiffness of solids in which a large Young's modulus value signifies a stronger resistance of the material against deformation. Therefore, the obtained Young's modulus value of the Sr_2ScBiO_6 indicates the degree of stiffness

Table 1 Calculated lattice parameter a (Å), bulk modulus B, its derivative B_P, the minimum total energy E_{tot}, energy of cohesion E_{coh}, enthalpy of formation E_f and bond length (Å) by different exchange–correlations (LDA, PBE, WC, PBEsol)

XC	a (Å)	V (a.u.^{3})	B (GPa)	B_P	E_{tot} (Ry)	E_c (eV per atom)	E_F (eV per atom)	Bader charge
LDA	8.19	928.40	159.59	5.04	−58 268.517946	5.20	−2.642	Sr = 1.61
PBE GGA	8.36	988.78	128.20	5.00	−58 314.926975			Sc = 1.98
WC GGA	8.27	955.80	143.29	5.11	−58 307.921573			Bi = 2.59
PBEsol	8.274	955.88	141.53	4.36	−58 291.162091			O = −1.29
Ref. 30	8.44		143.04	4.30				

Table 2 Calculated values of elastic constants C_{11}, C_{12}, C_{44} in (GPa), bulk modulus B (GPa), shear modulus G (GPa), Young's modulus Y (GPa), Poisson's ratio ν, Zener anisotropy factor (A), B/G ratio, Cauchy pressure ($C_{12}-C_{44}$), Debye temperature (θ_D (K)) and melting temperature T_m (K) for Sr_2ScBiO_6 compound by PBE-GGA

Parameters	Sr_2ScBiO_6	Ref. 30
C_{11} (GPa)	271.54	334.14
C_{12} (GPa)	91.65	92.46
C_{44} (GPa)	79.21	27.14
B (GPa)	128.30	
G (GPa)	89.53	
Y (GPa)	217.90	
B/G (GPa)	1.43	
U (GPa)	0.30	
Σ	0.21	
A (GPa)	0.88	
C_p	12.44	
V_t (m s^{-1})	3628.5	
V_l (m s^{-1})	6363.98	
V_m (m s^{-1})	4023.70	
θ_D (K)	494.36	
T_m	2083	

of the compound. The Pugh's ratio (B/G) was measured to compute the brittleness/ductileness of Sr_2ScBiO_6. In general, a material is ductile when the B/G is over 1.75 and *vice versa* (<1.75 = brittle).[45] Thus, the Sr_2ScBiO_6 was considered brittle in nature, given that the B/G ratio is lower than 1.75. Furthermore, Cauchy pressure (C_p) provides vital insights regarding the type of bonds and is represented by the following expression: $C_p = C_{12} - C_{44}$.[46] Basically, a negative C_p suggests a dominant presence of covalent bonds in the material, while a positive C_p value signifies that the material is composed mainly of ionic bonds. Based on the results, the Sr_2ScBiO_6 recorded a positive C_p value, confirming a dominant presence of ionic bonds in the compound. Similar to Pugh's ratio, Poisson's ratio (σ) classifies crystalline materials as brittle or ductile. A material is considered brittle or ductile depending on the separation line of $\sigma = 0.26$ ($\sigma < 0.26$ = brittle; $\sigma > 0.26$ = ductile). Table 2 indicates that the Poisson's ratio value of Sr_2ScBiO_6 is 0.21. Thus, the Sr_2ScBiO_6 crystal was classified as a brittle compound according to Poisson's ratio value, which was similar to the predicted Pugh's ratio. Apart from that, Poisson's ratio reflects the crystal's resistance to shearing force. A smaller Poisson ratio indicates that the material is more stable against shearing. In addition, a material is stable under a noncentral or central force; based on Poisson's ratio, one may anticipate the nature of the force that contributes to the material's stability. Generally, a compound possessing Poisson's ratio of 0.25–0.50 is categorised as stabilised by the central force, termed a central force crystal. In contrast, a material that possesses a Poisson's ratio beyond the fixed range is categorised as stabilised by the non-central force and is referred to as a non-central force crystal.[47] Based on the findings, the Sr_2ScBiO_6 is a noncentral crystal with a Poisson's ratio of 0.21. The elastic anisotropy level was also evaluated based on the amount of deviation from unity. A Zener anisotropic factor $A = 1$ refers to isotropic materials.[24] According to the results in Table 2, the Sr_2ScBiO_6 was classified as anisotropic compound. Furthermore, longitudinal velocity (ν_l), transverse velocities (ν_t) and average velocity (ν_m) were calculated from the expressions-

$$\nu_l = \sqrt{\frac{3B + 4G}{3\rho}} \tag{11}$$

$$\nu_t = \sqrt{\frac{G}{\rho}} \tag{12}$$

$$\nu_m = \left[\frac{1}{3}\left(\frac{2}{{\nu_l}^3} + \frac{1}{{\nu_t}^3}\right)\right]^{-(1/3)} \tag{13}$$

The Debye temperature was measured to estimate the maximum possible temperature value of the crystal under the normal vibration model

$$\theta_D = \frac{\hbar}{k_B}\left[\frac{3n}{4\pi}\left(\frac{N_{A\rho}}{M}\right)\right]^{-1/3} V_m \tag{14}$$

The symbols N_A, k_B, $\hbar$, and ρ, denote Avogadro's number, Boltzmann constant, Planck's constant, and density, respectively. The Debye temperature value also relates the elastic properties of solids to their thermodynamic features, such as vibrational entropy, melting point, and specific heat, making it an essential parameter of solids.[48] Table 2 lists the results of the calculated parameters. The Sr_2ScBiO_6 recorded a high Debye temperature value of 494.36 K, which indicates the huge lattice thermal conductivity of the compound. The Debye temperature also explains the hardness of solids, which is referred to as the Debye hardness. As shown in Table 2, the Sr_2ScBiO_6 has a high Debye hardness (494.36 K). The melting temperature was calculated based on the expression

$$T_m\ (\mathrm{K}) = [553\ (\mathrm{K}) \mp (5.911)C_{11}]\ \mathrm{GPa} \mp 300\ \mathrm{K} \tag{15}$$

The obtained melting temperature is 2083 ± 300 K.

3.3 Electronic properties

It is critical to evaluate the energy band structure of materials in order to have a better understanding of the material before it can be used in possible technological applications. Therefore, energy band dispersion is used to identify materials as insulators, semiconductors, semimetals, or metals. Fig. 3(a)–(f) presents the computed energy band structure of the first Brillouin zone with high symmetry k-point path W–L–G–X–W–K of the Sr_2ScBiO_6 compound using the LDA, PBE-GGA, WC-GGA, PBE-sol, TB-mBJ and mBJ + SOC without/with SOC approach. According to the TB-mBJ calculations in Table 3, the Sr_2ScBiO_6 exhibited an indirect bandgap of 3.327 eV between the minima of the conduction band (CB) at the X symmetry point and the maxima of the valence band (VB) at the Γ symmetry point. It is apparent from Fig. 3(a)–(f) that the mBJ functional delivers larger energy gap in comparison to the other approximation without altering the electronic bands. The band gap values from

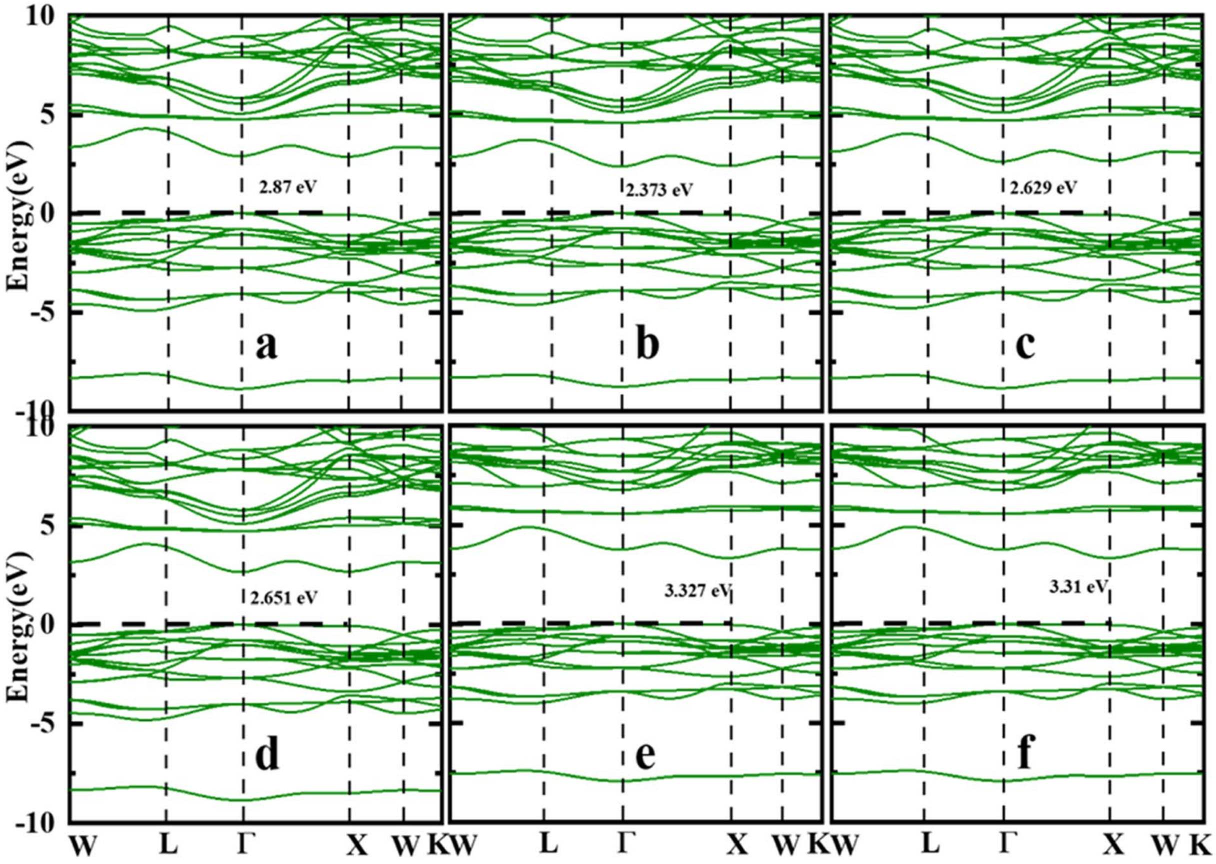

Fig. 3 Calculated band structure of Sr_2ScBiO_6 (a) LDA (b) PBE-GGA (c) WC-GGA (d) PBEsol (e) TB-mBJ (f) mBJ + SOC.

Table 3 Calculated energy bandgap (in eV) by different potentials LDA, PBE, WC-GGA, PBEsol, mBJ, and mBJ + SOC

Properties	LDA	PBE	WC-GGA	PBEsol	mBJ	mBJ + SOC
Sr_2ScBiO_6	2.874	2.373	2.629	2.651	3.327	3.319
Ref. 30		1.077			1.837	

Fig. 3(a)–(f) are found to be in the range of 2.373 eV to 3.327 eV for Sr_2ScBiO_6 by different exchange–correlation functions. Our findings are in good agreement with the published experimental value as well as the theoretical value in ref. 23–32 and 49–51. Due to the presence of heavy element Bi, the SOC effect was included to accurately describe the band structures. A drastic change occurred in the electronic bandgap due to the SOC effect, which led to a decrease in the bandgaps.

A thorough comparison of the electronic structure by different exchange–correlation functional *i.e.*, LDA, PBE-GGA, WC-GGA, PBEsol, TB-mBJ and mBJ + SOC was carried out by determining the Total Density of States (TDOS) spectra of the Sr_2ScBiO_6 using the TB-mBJ method between the −10 to 10 eV energy range, as shown in Fig. 4(a)–(f). The main characteristics of the total DOS curves in the VB and CB of Sr_2ScBiO_6 appear to be identical to one another, regardless of the method used for exchange–correlation potential in the calculations shown in Fig. 4(a)–(f). In the current DFT calculations carried out using the LDA and GGA technique, theoretical bands created by the Bi 5p and O 2p states are shown in this figure to have significantly shifted bandgaps (Table 3). There was a significant underestimation of the energy band gap obtained using the GGA approach. The mBJ approach has a significant impact on improving the E_g value, increasing it by up to 3.327 eV. This magnitude is quite consistent with prior theoretical investigations.

From Partial Density of States (PDOS) spectra depicted in Fig. 5, it is clear that the valence bands of the Sr_2ScBiO_6 were formed through the combination of the Bi 5s, and O 2p orbitals within an energy range of −8.00 to −7.35 eV. Besides, the valence band group in the Sr_2ScBiO_6 between −4.14 to −2.28 eV and −4.11 to 0 eV were due to the Bi 6p/5d and O 2p orbitals. As a result, the O 2p states predominated the valence band group at a range of −0.94 eV to Fermi level. Meanwhile, the O 2p states had little impact in the lower conduction bands, where the Bi 7s and Sc 3d states predominated. However, the Sr_2ScBiO_6's unoccupied bands produced Bi 6p, Sc 3d, and O 2p states in the energy range from 6.05 to 9.96 eV. In the conduction band, the Sc/Sc atom produces bands with energies ranging from 5.47 to 10 eV. The consequence of the hybridization with a minor contribution of Bi and O atoms (Table 4).

Charge density and its distribution plot can be used to determine the bonding properties of compounds.[29,50] Along the body diagonal plane, Fig. 6(a) and (b) depicts the spatial charge

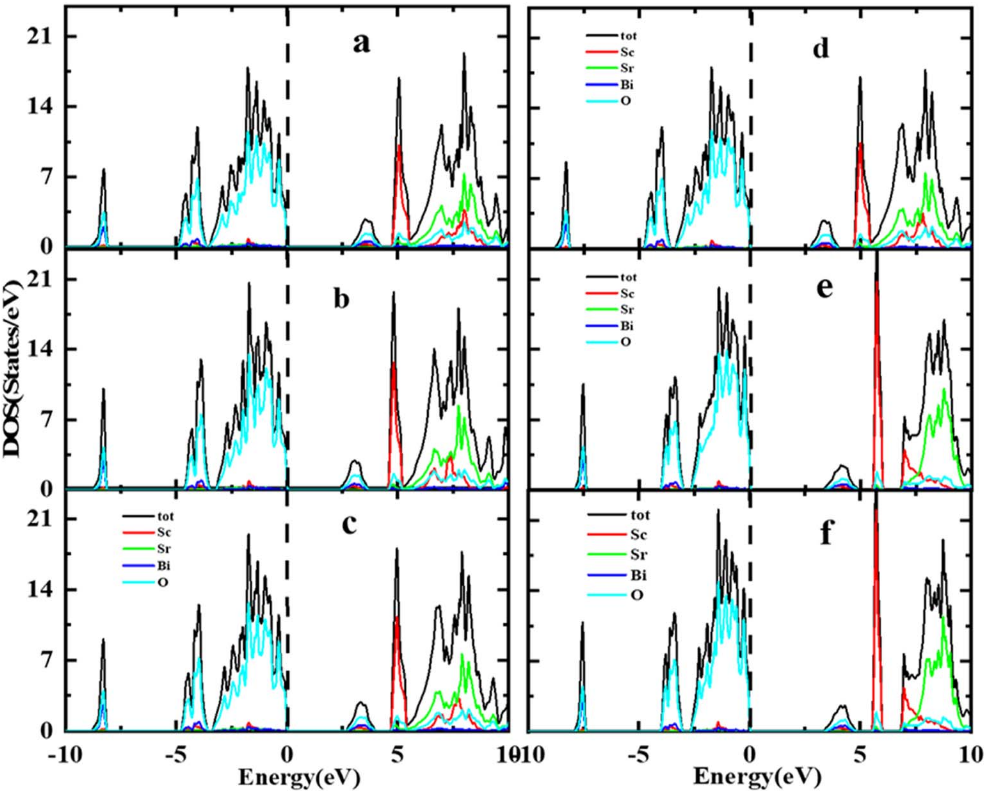

Fig. 4 (a–f) Comparison of the distribution of total density of states (TDOS) *via* local density approximation, generalized gradient approximation (GGA), and GGA + mBJ approximations.

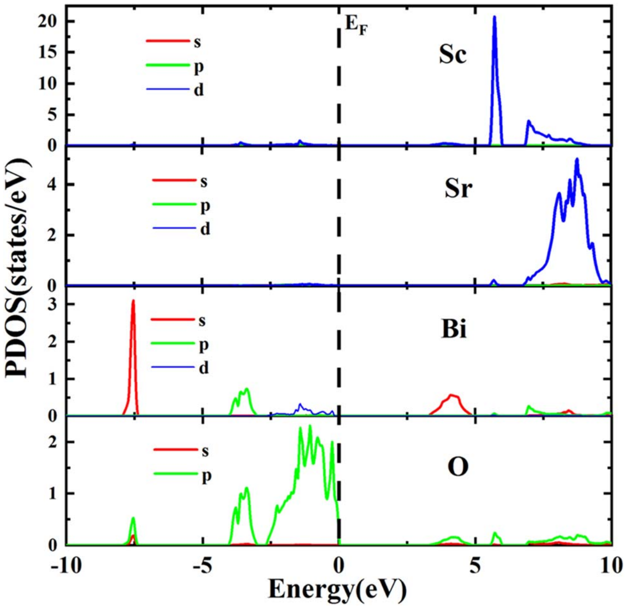

Fig. 5 Atomic and orbital density of states distribution of Sr_2ScBiO_6 by GGA + mBJ method.

configuration for the oxide-based double perovskite. The charge distributions of the Sr and Sc atoms are perfectly spherical, with no overlap between the charge contours of the O atom. It was discovered that there was an ionic bond between the Sr and Sc and the O atom. The charge distribution of the Bi, on the other hand, fluctuates from perfectly spherical to deformed, resulting in covalent bonding with the O atom which is also verified from the Bader charge analysis O accepts the electrons from the Bi network as presented in Table 1.

Table 4 Calculated optical properties of by TB-mBJ

Sr_2ScBiO_6	Material property	Sr_2ScBiO_6	Ref. 30
Optical properties	$\varepsilon_1(0)$	3.49	3.32
	$n(0)$	1.86	1.82
	$R(0)$	0.09	0.08

3.4 Optical properties

This section examines the interaction of electromagnetic radiation with Sr_2ScBiO_6 and its application in optoelectronics. Given that the dielectric function describes the interaction between the photons and electrons of a material, an insignificant wave vector portrays the linear response of the system to the incident light. The interaction is conveyed as a complex quantity following Cohen and Ehrenreich's equation

$$\varepsilon(\omega) = \varepsilon_1(\omega) + i\varepsilon_2(\omega) \tag{16}$$

where $\varepsilon_1(\omega)$ and $\varepsilon_2(\omega)$ refer to the real and imaginary component of the dielectric function ($\varepsilon(\omega)$). Inter-band and intra-band

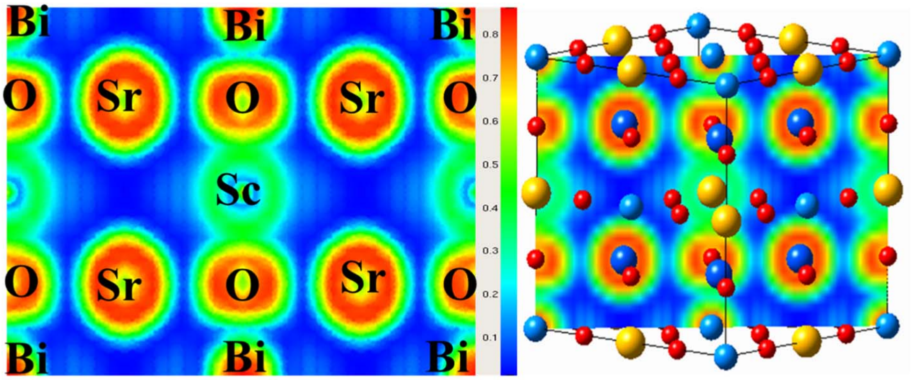

(a) (b)

Fig. 6 (a and b) Electron localization function profile of Sr_2ScBi along 110 plane.

transitions that are dependent on DOS and the momentum matrix P are used to compute the imaginary portion $\varepsilon_2(\omega)$ which displays realistic transitions along k-vectors from the occupied to the unoccupied states over the Brillouin zone (BZ) computed as

$$\varepsilon_2(\omega) = \frac{e^2\hbar}{\pi m^2\omega^2}\sum\int \left|M_{\nu,c}(k)\right|^2 \delta[\omega_{\nu c}(k)-\omega]\mathrm{d}^3k \qquad (17)$$

where c_k and ν_k are the crystal wave functions in relation to the CB and VB along the crystal wave vector k, and p denotes the moment matrix element between the band states of and under the crystal momentum k. Similar to how $\varepsilon_1(\omega)$ is determined

$$\varepsilon_1(\omega) = 1 + \frac{2}{\pi}P\int_0^\infty \frac{\omega'\varepsilon_2(\omega')\mathrm{d}\omega'}{\left(\omega'^2-\omega^2\right)} \qquad (18)$$

In this study, the dielectric function, $\varepsilon(\omega)$ was analysed to determine the response of the Sr_2ScBiO_6 to the incident light. The $\varepsilon_1(\omega)$ and $\varepsilon_2(\omega)$ were applied to compute the remaining optical parameters. The optical variables of the estimated equilibrium structure are shown in Fig. 7(a)–(f), together with the incident energy of the radiation from 0 to 12 eV. Fig. 7(a) shows the real and imaginary components of the dielectric function, $\varepsilon(\omega)$. The static value of $\varepsilon_1(\omega)$, particularly at $\varepsilon_1(0)$, is 3.47. The result in Fig. 7(a) also shows that the $\varepsilon_1(\omega)$ of Sr_2ScBiO_6 initially elevated with the increase in the incident electromagnetic radiation energy, subsequently generating two $\varepsilon_1(\omega)$ peaks at approximately 4.43 eV and 5.83 eV in the UV region. Afterwards, the $\varepsilon_1(\omega)$ declined swiftly and reached a negative value at 9.76 eV. Thus, the dielectric nature of the Sr_2ScBiO_6 demonstrated metallic properties when the $\varepsilon_1(\omega)$ accedes a negative value. Furthermore, Fig. 7(a) depicts that the threshold energy, $\varepsilon_2(\omega)$ of the Sr_2ScBiO_6 was approximately 4.0 eV, indicating the optical bandgap of the compound. The data was marginally close to the predicted energy bandgap of the electronic band structure (3.32 eV), demonstrating the extreme precision of the present findings.

The optical transition between the valence band maximum (VBM) and the conduction band minimum (CBM) occurred at approximately 3.32 eV. Conversely, the curve accelerated beyond this point as a result of the sudden increment in the number of points that contributed to the $\varepsilon_2(\omega)$. Besides, two major peaks were detected in the Sr_2ScBiO_6 spectrum at 4.82 eV and 7.59 eV as a result of the electronic transition from the occupied O 2p state to the unoccupied Bi 6s state in the valence band. Additionally, Fig. 7(b) illustrates the $n(\omega)$, which is an optical factor that describes the penetration of light through a material and its absorption potential.[60] When $n(0)$, the static value of Sr_2ScBiO_6 was 1.86. As shown in the graph, the increase in $n(\omega)$ caused the energy of the incident radiation to increase, which peaked at 4.35 eV. However, the $n(\omega)$ spectrum declined drastically as photon energy increased until it reached the minimal value of less than 1 in the UV region. Moreover, the local maxima of the extinction coefficient, $k(\omega)$, of the Sr_2ScBiO_6 (Fig. 7(b)) was approximately 1.44 at 8.51 eV, which coincides with the zero value of $\varepsilon_1(\omega)$. According to Fig. 7(a), it can be deduced that the $n(\omega)$ spectra correspond to the $\varepsilon_1(\omega)$ spectra.

In addition, Fig. 7(c) depicts $\sigma(\omega)$ spectra of the incident radiation energy, which refers to the photo-electrons conduction under radiation energy. The $\sigma(\omega)$ of Sr_2ScBiO_6 began to increase beyond 3.32 eV and reached a maximum $\sigma(\omega)$ of 5459.41 Ω^{-1} cm^{-1} at 8.24 eV. Meanwhile, Fig. 7(d) presents the varying absorption coefficient, $\alpha(\omega)$ of the Sr_2ScBiO_6 as a function of the incident photon energy. In general, the $\alpha(\omega)$ represents the absorbed amount of the incident light energy by the unit thickness of the material. A higher absorption coefficient value denotes that a material transports electrons more efficiently from the VB to the CB. The results showed a wide range of absorption regions from vis to UV with a maximum $\alpha(\omega)$ of 124.95×10^4 cm^{-1} at 8.53 eV. In addition, the absorption edge of the Sr_2ScBiO_6 was 3.32 eV, which is in line with the indirect transition between the CBM and the VBM. Based on Fig. 7(a), the $\alpha(\omega)$ was almost zero in the same region, where the optical conductivity, $\sigma(\omega)$ was also zero. The findings also revealed that the $\sigma(\omega)$ achieved a maximum value when the absorption reached its peak. Therefore, the outcome of this study demonstrated the suitability of the Sr_2ScBiO_6 in vis and UV-based optoelectronic devices.

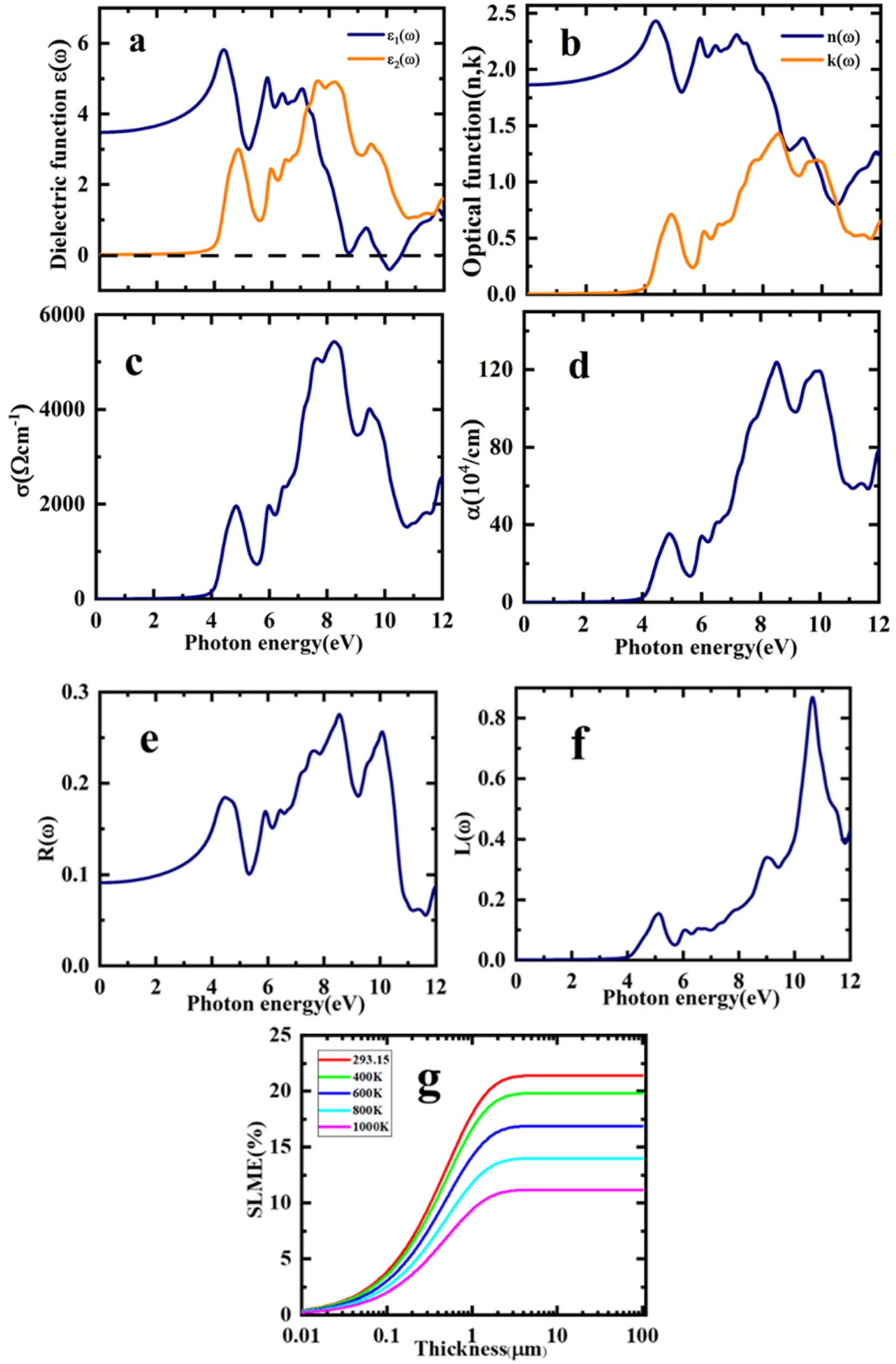

Fig. 7 Optical properties of Sr_2ScBiO_6 by mBJ (a) dielectric function (b) optical function (c) optical conductivity (d) absorption coefficient (e) reflectivity (f) energy loss function (g) SLME.

The optical value, $R(\omega)$ of the Sr_2ScBiO_6 as a function of the incident radiation energy is portrayed in Fig. 7(e). Based on the figure, the calculated zero-frequency $R(0)$ of the Sr_2ScBiO_6 was 7.66%. The increment in the incident photon energy leads to the increased value $R(\omega)$, which achieved a maximum value of approximately 72.3% in the UV region at 8.56 eV. Although the

$R(\omega)$ fluctuated, the value remained minimum in the energy bandgap range. Overall, the transparency of the incident radiation energy up to the E_g demonstrates the promising properties of Sr_2ScBiO_6 in the production of lenses. The results in Fig. 7(f) also present the calculated value of the electron loss function, $L(\omega)$. The plasma resonance properties were detected by the $L(\omega)$ peaks with a maximum resonant energy loss of 0.87 at 10.63 eV.

The "spectroscopic limited maximum efficiency (SLME)" technique may be used, as stated, to examine the photovoltaic efficiency of a material used as an absorber layer in a solar cell. SLME simulation framework assesses the Shockley–Queisser model for calculation of solar cell power conversion efficiency.[52]

$$i.e., \mathrm{SLME}, \eta = \frac{\text{maximum output power density}(P_{\max})}{\text{total incident solar density}(P_{\text{in}})} \quad (19)$$

$$P_{\max} = \max\left\{I_{\text{SC}} - I_0 \exp\left[\frac{eV}{kT} - 1\right]\right\} \quad (20)$$

where I_{SC}, I_0, e, V, k, T embodies short circuit current density, reverse saturation current, the electronic charge, potential over the absorber layer, Boltzmann's constant and temperature of the device, respectively. The global solar spectra (AM-1.5 G), fundamental, and direct permissible band gap (E_g) of the photovoltaic material are the input variables to evaluate the SLME analysis. The calculated SLME for double perovskite Sr_2ScBiO_6 at different temperatures and thickness is presented in Fig. 7(g). SLME diminishes from 21.5% to 11.3% for the explored Sr_2ScBiO_6 as the temperature of the device is increased from 293.15 K to 1000 K, while it gradually rises with the thickness of the material and becomes constant after 1.0 µm, as shown in Fig. 7(g). Our computed SLME study, shows that Sr_2ScBiO_6 has an SLME of 21.5% at 293.15 K, which is a suitable value for the solar cells and therefore the investigated DH could be a budding contender for energy conversion techniques.

3.5 Thermodynamic properties

Utilising the quasi-harmonic approach (QHM), the thermodynamic characteristics of the Sr_2ScBiO_6 perovskites and their relationship to temperature and pressure are investigate. This necessary data is evaluated by the GIBBS2 programme[53–55] at the expense of optimised *E*–*V* data obtained from the Birch–Murnaghan equation. It is possible to evaluate the temperature as well as pressure dependency of thermodynamic characteristics using the DFT simulation. The benefit of the calculations is the simplicity with which one can estimate and estimate how these parameters would behave under severe circumstances.

Fig. 8(a) illustrates the graphical fluctuation in volume-specific heat capacity (C_V) with changing temperature at various pressures within the confines of the QHM approximation. When the pressure is constant, the C_V rises as the temperature rises, but T^3-law states that changes are sharper at lower temperatures.[38] C_V becomes equal to $3nR$ at higher temperatures (Dulong–Petit's limit). At normal temperature, the C_V drops from 367.2 J kg−1 K^{-1} at 0 GPa to 322.2 J kg^{-1} K^{-1} at 120 GPa, but at any given temperature, the C_V exhibits a declining tendency. When pressure is applied, some vibrations are diminished, but the inverse relationship between temperature and pressure is brutally strengthened. The smoothness of the C_V variation supports the stability of thermodynamics. Thermal expansion results from the inter-atomic bonds elongating as a result of the phonon frequency increasing as the temperature rises.

The change in a solid's size as a function of temperature is represented by the thermal expansion coefficient (α). The majority of solids soften to some extent, whereas weakly bound materials expand to a higher extent. Fig. 8(b) illustrates how the aforementioned coefficient changes with pressure and temperature. As the temperature rises, displays a saturation value. But at a lower temperature, it rises quickly and takes on a characteristic resembling that of C_V. Table 5 lists the reported values for each parameter's room temperature. The comparison with the experimental data indicates a slight discrepancy, which might be the effect of restricting the parameter estimation to only one harmonic level.

Following that, we have calculated the Debye temperature (θ_D), that serves as a reliable measure of hardness; compounds with large θ_D are comparatively stiffer than those with low θ_D. Fig. 8(c) graphically depicts the behaviour fluctuation in θ_D with increasing temperature and altered pressures. θ_D slowly falls as temperature increases. There is a nearly constant Debye temperature at the low temperature because high-frequency phonon modes are locked. Since atomic bonding is strengthened by pressure, θ_D also rises as pressure increases. Table 5 provides the value of θ_D for room temperature. The perovskites could be exploited for applications even at greater temperatures, according to the high value of Debye temperature.

Entropy (S) describes the dispersion of energy and matter; entropy can be regarded as a measure of a system's disorder. The fluctuations of entropy S as a function of temperature at various pressures are depicted in Fig. 8(d). The graphs connecting to them show that the entropy rises noticeably with temperature; also, the entropy is more sensitive to changes in temperature than changes in pressure. Entropy is slightly higher at low pressure than it is at high pressure for a given temperature. The obtained values of the entropy S at 0.0 GPa and 300 K are 236.84 J mol^{-1} K^{-1}.

3.6 Thermoelectric properties

The majority of the world's energy needs are now met by nonrenewable fossil fuels. However, due to the unending need for energy, the world is in the grip of an energy crisis. As a result, scientists have spent a significant amount of effort investigating novel materials capable of directly producing electrical energy from waste heat. Thermoelectric materials have sparked considerable attention in this field due to their effective capacity to transform waste heat into power. Thermoelectric materials are helpful for generating power in a variety of applications in energy-based technologies. The increasing worldwide energy demand, along with significant energy loss due to heat, has compelled the scientific community to research innovative materials and develop effective strategies for generating useable

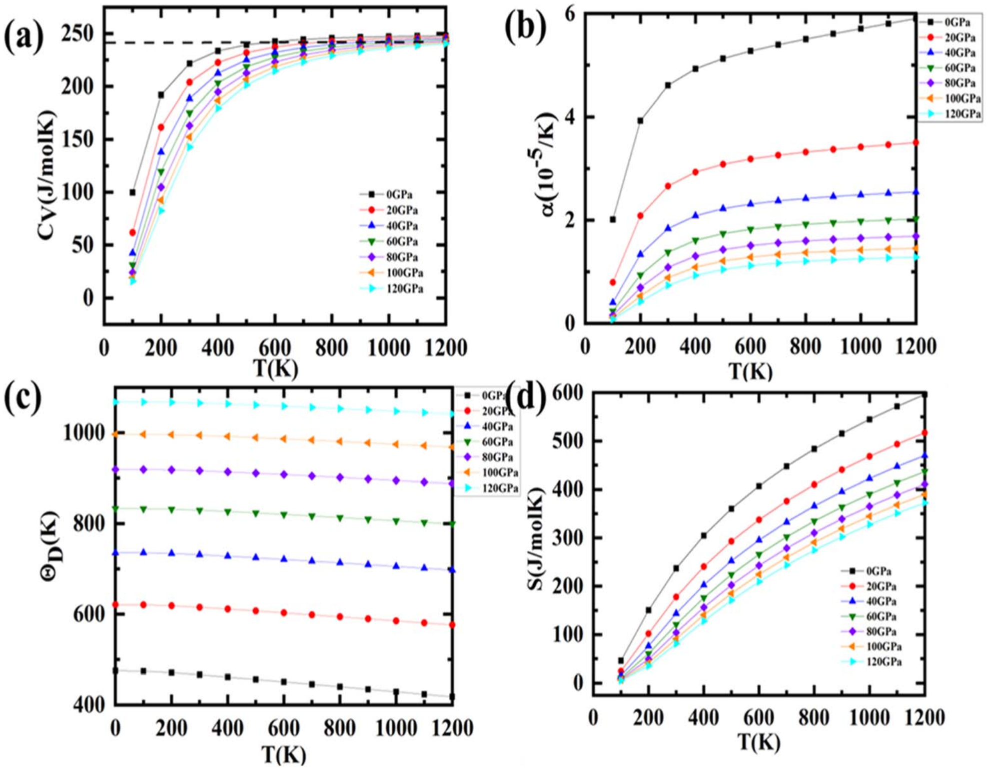

Fig. 8 Variation in thermodynamic parameters with temperature and pressure *viz.* (a) specific heat (C_V); (b) thermal expansion (c) entropy and (d) Debye temperature.

Table 5 Values of different thermodynamic parameters at room temperature and zero pressure

	Material property	Present study
Optical properties	C_V (J kmol^{-1})	99.7
	α (10^{-5} K^{-1})	4.61
	S (J kmol^{-1})	236
	θ_D (K)	466

electrical energy from heat waste. Because the TB-mBJ method determines a unique energy bandgap value, the thermoelectric characteristics of Sr_2ScBiO_6 were determined using the BoltzTrap algorithm[40] after the TB-mBJ band structure computation. Under the constant relaxation time approximation, the relaxation time is kept constant ($\tau \sim 10^{-14}$ s), which is especially effective in forecasting the different thermoelectric characteristics.

An efficient thermoelectric material ought to possess an extremely high *ZT* value in proximity to unity, which is merely feasible when S & σ are high and κ_e is low. The Seebeck coefficient (S) is crucial in describing thermoelectric efficacy. Thus, we have deliberated the thermal dependence of S as depicted in Fig. 9(a). It is imperative to be cited that the ratio of the variation in voltage to the corresponding temperature change is denoted as S.

The Seebeck coefficient has a reciprocal relationship with carrier concentration, as shown by the formula below.

$$S = \left(\frac{8\pi^2 k_B}{3eh^2}\right) m^* T (\pi/3n)^{2/3} \tag{21}$$

It is perceptible from Fig. 9(a) that S diminutions with temperature for Sr_2ScBiO_6. This high value in S may be explained in conjunction with the size of the band gap, which varies with temperature and carrier concentration. It should be noted that the Seebeck coefficient (S) is dependent on the geometry of the DOS around VBM and CBM. Temperature changes can have a significant effect on the shape of DOS. The room temperature S values are noticed to be 234 μV K^{-1} for Sr_2ScBiO_6. The reduction in the value of S with temperature is due to the annulment of induced Seebeck voltage because of the drift of charge carriers. The positive value of S shows the p-type behaviour of this compound as represented in Table 6.

The power factor ($S^2\sigma/\tau$) is a significant quantity which reflects both the efficiency and power generation of thermoelectric materials. For both n-type and p-type doping, it is displayed as a function of temperature (Fig. 9(b)). As seen from this figure that the PF displays rise with increasing temperature and reaches an optimal value of $\sim 2.87 \times 10^{11}$ W m^{-1} K^{-2} s^{-1} at $T = 1200$ K. This computed value is definitely higher than similar thermoelectrics such as Dirac semimetals Ca_3PbO and Ca_3SnO,[56] topological semimetal ZrTe,[57] half-Heusler NbCoSn[58] *etc.*

The figure of merit (*ZT*) depends on Seebeck coefficient (S), electrical conductivity (σ/τ), and the total thermal conductivity

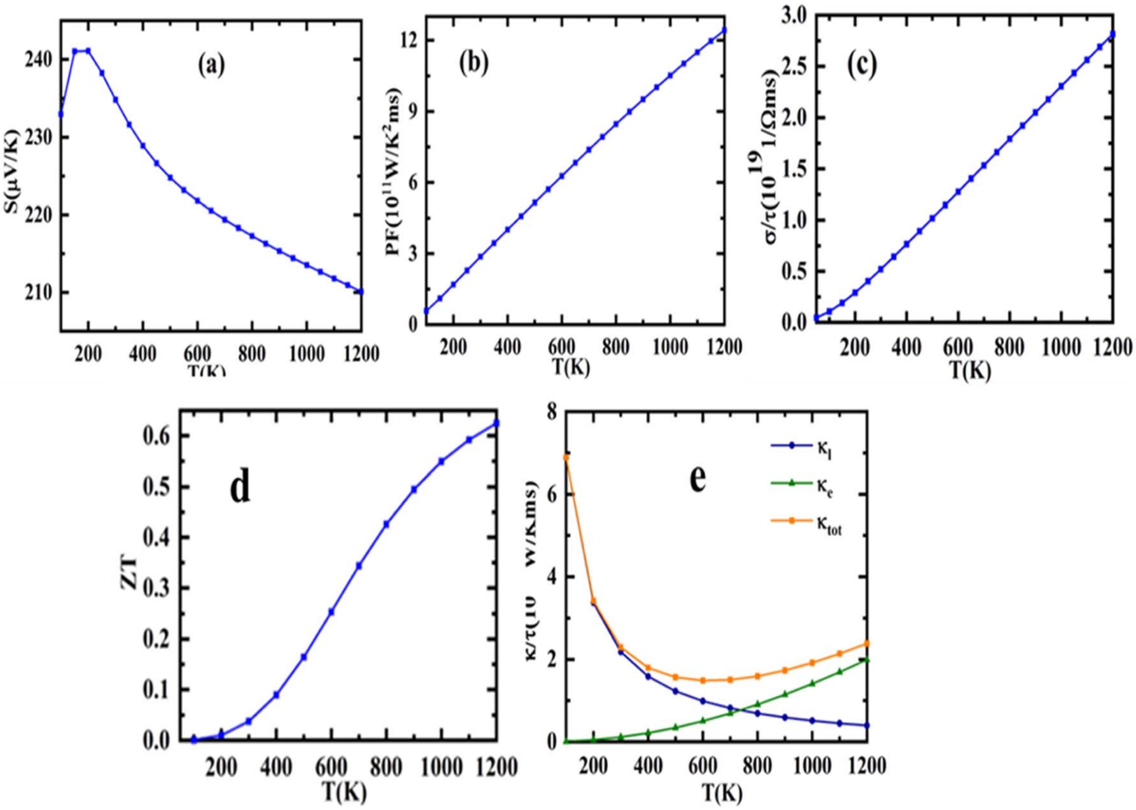

Fig. 9 Representation of variation in (a) Seebeck coefficient, (b) power factor (c) electrical conductivity (d) total thermal conductivity (e) figure of merit (*ZT*) with temperatures.

(κ_{tot}). Here the total thermal conductivity (κ_{tot}) is taken as the sum of the electrical conductivity (κ_{e}) and of the lattice thermal conductivity (κ_{l}).

$$ZT = \frac{S^2\sigma T}{\kappa_{\text{e}} + \kappa_{\text{l}}} = \frac{S^2\sigma T}{\kappa_{\text{tot}}} \tag{22}$$

Moved by the large value of S, σ/τ and minimal k/τ values, we have also evaluated the figure merit (*ZT*) Fig. 9(c). It is obvious from Fig. 9(c) that the *ZT* of Sr_2ScBiO_6 is increasing with temperature. This variance rate, however, is relatively low. The values of *ZT* at room temperature are found to be 0.037 for Sr_2ScBiO_6 and maximum *ZT* are found to be 0.62 at 1200 K. The larger value of *ZT* suggests that the investigated compound possesses promising thermoelectric behaviour. The declining pattern of the *ZT* values in Fig. 9(c) may be explained by the temperature dependency of the band gap. Eqn (16) illustrates the relationship between band gap and temperature.[41]

$$E_{\text{g}}(T) = E_{\text{g}}(0) - \frac{\alpha T^2}{T + \beta} \tag{23}$$

The temperature variation of electronic conductivity σ/τ for Sr_2ScBiO_6 are presented in Fig. 9(d). We can realize from Fig. 9(d) that σ/τ has a linear relation with temperature because of this semiconducting nature of Sr_2ScBiO_6. Thermal energy is widely recognised for its ability to generate charge carriers within a semiconductor. As a result, raising the temperature can increase the carrier concentration and related conductivity values. Furthermore, the growing a propensity of σ/τ is

Table 6 Calculated transport properties of by TB-mBJ

	Material property	Sr_2ScBiO_6	Ref. 30
Transport properties (300 K)	σ/τ $(\Omega\ \text{m s})^{-1}$ (10^{18})	5.21	1.27
	S (μV K)	234	241
	R_{H} $(10^{-8}\ \text{m}^3\ \text{C}^{-1})$	1.24	
	k_{e}/τ $(\text{W m}^{-1}\ \text{K}^{-1}\ \text{s}^{-1})$ (10^{15})	0.11	
	k_{L}/τ $(\text{W m}^{-1}\ \text{K}^{-1}\ \text{s}^{-1})$ (10^{15})	2.18	
	k/τ $(\text{W m}^{-1}\ \text{K}^{-1}\ \text{s}^{-1})$ (10^{15})	2.29	
	PF (10^{11}) $(\text{W K}^{-2}\ \text{m}^{-1}\ \text{s}^{-1})$	2.87	
	ZT_{e}	0.037	

compatible with band theory. In addition, similar σ/τ pattern is reported by Sajad *et al.*[24] and Manzoor *et al.*[30] The σ/τ values are found to be $5.21 \times 10^{18}\ \Omega^{-1}\ \mathrm{m}^{-1}\ \mathrm{s}^{-1}$ for Sr_2ScBiO_6 at the ambient temperature. The large value of σ/τ ($10^{18}\ \Omega^{-1}\ \mathrm{m}^{-1}\ \mathrm{s}^{-1}$) suggests they are exciting thermoelectrics.

The electronic thermal conductivity (κ_e/τ) is plotted in Fig. 9(e) over a wide range of temperatures (100–1200 K) depicts that the κ_e/τ upsurges as the temperature rises. The optimal values of κ_e/τ for Sr_2ScBiO_6 is found to be $1.99 \times 10^{15}\ \mathrm{W\ m^{-1}\ K^{-1}\ s^{-1}}$, at 1200 K. The thermal conductivity is found to be in direct proportion with the electrical conductivity in accordance with the Wiedemann–Franz law *i.e.*, $\kappa_e = L\sigma T$, where L is Lorentz number. Achieving minimal lattice thermal conductivity is crucial for TE materials since minimizing thermal conductivity produces a high ZT value. The lattice thermal conductivity can be computed with the help of Slack's equation:[59]

$$\kappa_l = A\frac{M\delta\theta_D{}^3}{\gamma^2 n^{2/3} T} \tag{24}$$

where M represents the atomic mass, δ denotes cube root of the volume of the unit cell, θ_D is the Debye temperature, γ – Grüneisen parameter, n – the number of atoms per unit cell and T is the temperature and $A = 3.04 \times 10^{-6}$.[60] The temperature dependence of κ_l for the studied double perovskite has been demonstrated in Fig. 10(e). Due to the rise in scattering of phonons with increase in temperature, κ_l diminishes with the temperature.

After this, we have made an effort to study the thermal dependence of total thermal conductivity and presented in Fig. 9(e). It can be clearly seen in Fig. 9(e) that κ/τ varies in direct proportion with temperature, which agrees well with the study reported by Bendjilali *et al.*[49] and Bhamu *et al.*[61] The value of κ/τ is found to be $2.29 \times 10^{15}\ \mathrm{W\ m^{-1}\ K^{-1}\ s^{-1}}$ for Sr_2ScBiO_6 at ambient conditions. It is imperative to be cited here that the comparatively lower value of κ/τ reveals that Sr_2ScBiO_6 can be proficient candidate for thermoelectrics.

The chemical potential dependence of transport properties have been studied to compute the thermoelectric properties of the Sr_2ScBiO_6 at three different temperatures of 300, 600, and 900 K as presented in Fig. 10(a)–(e). The Fermi level is set at 0 eV represented by the dotted lines. The chemical potential is depicted by positive values for n-type doping whereas negative values for p-type doping.

As illustrated in Fig. 10(a), Sr_2ScBiO_6 reported the lowest electrical conductivity value in the n-type doping zone and decreased when the temperature reached 600 and 900 K. It also observed a maximum S value in the electron-doped region at about 3044.06 μV K^{-1} (0.84 eV) while hole doped region at about −2814.01 μV K^{-1} (2.54 eV) at 300 K. Furthermore, the S value of Sr_2ScBiO_6 was around −203 μV K^{-1} at $\mu = 0$, and the positive value indicates that the compound is a p-type semiconductor in which the majority of the charge carriers are holes.

The PF of the compound Sr_2ScBiO_6 is also shown *vs.* temperature in Fig. 10(b). PF is frequently used to explore the

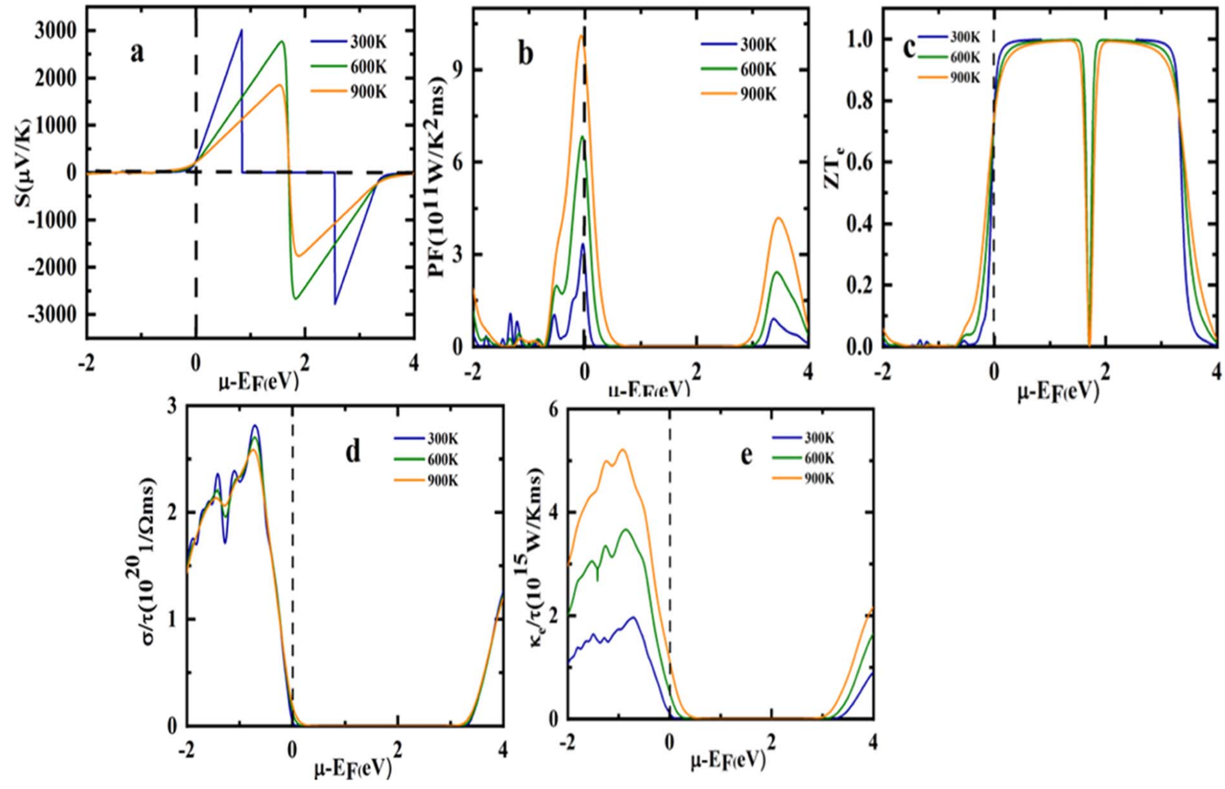

Fig. 10 Representation of variation in (a) Seebeck coefficient, (b) power factor (c) electrical conductivity (d) total thermal conductivity (e) figure of merit (*ZT*) with chemical potential at different temperatures.

capability of a compound to generate electric power. As seen in the figure, the compound's p-type doping region recorded a substantially higher PF value than the n-type. The PF value raised as the temperature elevated and the Sr_2ScBiO_6 combination attained the maximum PF value of around 10.14×10^{11} W m^{-1} K^{-2} s^{-1} (3.36×10^{11} W m^{-1} K^{-2} s^{-1}) at $\mu = -0.069$ (-0.044) at 900 K temperature (300 K).

The most important characteristic that governs the efficient performance of thermoelectric materials is *ZT*. It increases with the increase in electrical conductivity and *S* but decreases with the increment of κ. The *ZT* value of Sr_2ScBiO_6 is depicted as a function of chemical potential in Fig. 10(c). The maximum height of the Sr_2ScBiO_6 double perovskite measured a *ZT* value of close to 1 in the range, which is consistent with the highest *S* values, and increased with temperature. Sr_2ScBiO_6 attained a remarkably constant *ZT* value of 0.99 at the Fermi level despite various temperature influences. As a result, the Sr_2ScBiO_6's high *ZT* value denotes its semiconducting nature, which is favourable for the advancement of the field of thermoelectric technology.

The graph of electrical conductivity (σ/τ) *versus* chemical potential (μ) is shown in Fig. 10(d). In terms of the energy band gap, the material exhibited a low σ/τ in the μ range while a maximum σ/τ was achieved at higher chemical potential, relates to the p-type doping. In particular, the σ/τ rose to its highest value of 2.81×10^{20} Ω^{-1} m^{-1} s^{-1} from zero at -0.71 eV in the hole-doped region. Accordingly, the σ/τ was influenced by the DOS or transport distribution function but unaffected by the temperature change. Thus, it was evidenced that the σ/τ of the Sr_2ScBiO_6 double perovskite compound is temperature independent with an estimated σ/τ of 0.04×10^{20} Ω^{-1} m^{-1} s^{-1} under room temperature conditions (300 K).

Comparable with the electronic conductivity (σ/τ), the electronic thermal conductivity (κ_e) of the Sr_2ScBiO_6 compound was detected in the hole-doped region, as portrayed in Fig. 10(e). This was due to the connection between κ_e value and σ through the Wiedemann–Franz law, $\kappa_e = L\sigma T$, where L denotes the Lorentz number (2.44×10^{-8} J^2 K^{-2} C^{-2} for free electrons). The κ_e value corresponds to an increased temperature under a fixed pressure level. Additionally, an ideal thermoelectric material possesses a small κ/σ value, as stated in the Wiedemann–Franz law ($LT = \kappa/\sigma$).[62] According to Wiedemann–Franz's law, σ is nearly constant. Therefore, the increase in temperature relied on the enhanced κ_e value of the Sr_2ScBiO_6, which was around 0.77×10^{15} W m^{-1} K^{-1} s^{-1} at $\mu = 0$. Moreover, the *LT* ratio of the compound was in the order of 10^{-5} at room temperature ($\kappa/\sigma = 2.4 \times 10^{-5}$), highlighting the potential use of Sr_2ScBiO_6 as a ceramic material in electric generators, heat sensors, and refrigerators applications.

4. Conclusion

First principles based DFT technique and BoltzTrap simulations were used in this study to investigate the fundamental characteristics of Sr_2ScBiO_6 double perovskite. Sr_2ScBiO_6 was basically anisotropic and displayed good mechanical stability in terms of structural and elastic properties. Despite being regarded as a non-central force solid with brittleness and primarily consisting of covalent bonds, the compound Sr_2ScBiO_6. The electronic properties of Sr_2ScBiO_6 perovskite were calculated using different exchange potentials: LDA, PBE-GGA, WC-GGA, PBEsol-GGA, mBJ-GGA, with and without SOC. By including the SOC effect in the calculations, the bandgaps computed with the mBJ-GGA method were found to be in good agreement. In terms of its electrical characteristics, Sr_2ScBiO_6 was discovered to have an indirect bandgap of 3.327 eV and to be p-type semiconducting. Furthermore, the optical properties of the Sr_2ScBiO_6 were predicted to provide an active response and beneficial impact for various applications in the vis and UV range. Hence, S, κ_l, κ_e, PF, ZT_e and σ of Sr_2ScBiO_6 were calculated with exceptional precision with substantial power factor and *ZT* values, which is pivotal in achieving effective thermoelectric applications. The computed *ZT* values are 0.037 at ambient conditions. The excellent optoelectronics and thermoelectric properties reveal their usage in solar cell and thermoelectric generators.

Data availability

The raw/processed data can be made available with a reasonable request to the corresponding author.

Conflicts of interest

The authors declare that they have no known competing financial interests or personal relationships that could have appeared to influence the work reported in this paper.

Acknowledgements

The authors extend their appreciation to the Deanship of Scientific Research at King Khalid University, Saudi Arabia for funding this work through Large Groups Project under grant number RGP2/74/44.

References

1 M. H. Elsheikh, D. A. Shnawah, M. F. M. Sabri, S. B. M. Said, M. H. Hassan, M. B. A. Bashir and M. Mohamad, A review on thermoelectric renewable energy: principle parameters that affect their performance, *Renew. Sustain. Energy Rev.*, 2014, **30**, 337–355.
2 X. F. Zheng, C. X. Liu, Y. Y. Yan and Q. Wang, A review of thermoelectrics research–recent developments and potentials for sustainable and renewable energy applications, *Renew. Sustain. Energy Rev.*, 2014, **32**, 486–503.
3 H. J. Goldsmid and H. J. Goldsmid, *The Seebeck and Peltier Effects*, Morgan & Claypool Publishers, New York, NY, USA, 2017.
4 W. H. Steele, A new thermoelectric phenomenon, *Science*, 1893, **562**, 256.
5 D. Champier, Thermoelectric generators: a review of applications, *Energy Convers. Manag.*, 2017, **140**, 167–181.

6 N. Mingo, Thermoelectric figure of merit and maximum power factor in III–V semiconductor nanowires, *Appl. Phys. Lett.*, 2004, **84**, 2652–2654.

7 X. Xu, Y. Xu, J. Ma, Y. Yin, M. Fronzi, X. Wang and L. Bi, Tailoring electronic structure of perovskite cathode for proton-conducting solid oxide fuel cells with high performance, *J. Power Sources*, 2021, **489**, 229486.

8 S. Balasubramanian, D. S. Priyanka, M. Srinivasan and P. Ramasamy, Ab initio method to investigate perovskites BiXO3 (X= Be, Ca, Mg, Na, K, Li) for spintronics applications, *Solid State Sci.*, 2022, **126**, 106839.

9 D. S. Priyanka, M. M. S. Sirajuddeen, M. Srinivasan and P. Ramasamy, Spin polarized study of alkaline earth-cubic lead perovskites (PbXO3, X= Mg, Ca & Sr) for emerging spintronic technology, *J. Cryst. Growth*, 2022, **590**, 126699.

10 N. Nazir and M. Ikram, Tuning of the structural, morphological, dielectric, and magnetoresistance properties of Gd2NiMnO6 double perovskite by Ca doping, *Phys. B*, 2022, **632**, 413734.

11 S. Mishra, R. Choudhary and S. Parida, Structural, dielectric, electrical and optical properties of Li/Fe modified barium tungstate double perovskite for electronic devices, *Ceram. Int.*, 2022, **48**, 17020–17033.

12 A. U. Rahman, M. Aurangzeb, R. Khan, Q. Zhang and A. Dahshan, Predicted double perovskite material Ca2ZrTiO6 with enhanced n-type thermoelectric performance, *J. Solid State Chem.*, 2022, **305**, 122661.

13 A. A. Bhat, M. B. Zaman, J. H. Malik, K. A. Malik, I. Assadullah and R. Tomar, Facile Way of Making Hydrothermally Synthesized Crystalline SrSnO3 Perovskite Nanorods Suitable for Blue LEDs and Spintronic Applications, *ACS Omega*, 2021, **6**, 16356–16363.

14 P. Roy, I. Bose and T. Maiti, Synthesis and characterization of Sr2TiMO6 (M= Fe, Co) double perovskites for high temperature thermoelectric applications, *Integr. Ferroelectr.*, 2016, **174**, 34–42.

15 A. Aziz, S. A. Aldaghfag, M. Zahid, J. Iqbal, M. Yaseen and H. H. Somaily, Theoretical investigation of X2NaIO6 (X = Pb, Sr) double perovskites for thermoelectric and optoelectronic applications, *Phys. B*, 2022, **630**, 413694.

16 K. A. Parrey, S. A. Khandy, I. Islam, A. Laref, D. C. Gupta, A. Niazi, A. Aziz, S. G. Ansari, R. Khenata and S. Rubab, Electronic Structure, Optical and Transport Properties of Double Perovskite La2NbMnO6: A Theoretical Understanding from DFT Calculations, *J. Electron. Mater.*, 2018, **47**, 3615–3621.

17 B. Rameshe, M. Rajagopalan and B. Palanivel, Electronic structure, structural phase stability, optical and thermoelectric properties of Sr2AlM′O6 (M′ = Nb and Ta) from first principle calculations, *Comput. Condens. Matter*, 2015, **4**, 13–22.

18 S. A. Dar, R. Sharma, V. Srivastava and U. K. Sakalle, Investigation on the electronic structure, optical, elastic, mechanical, thermodynamic and thermoelectric properties of wide band gap semiconductor double perovskite Ba2InTaO6, *RSC Adv.*, 2019, **9**(17), 9522–9532.

19 S. Al-Qaisi, M. Mushtaq, J. S. Alzahrani, H. Alkhaldi, Z. A. Alrowaili, H. Rached, B. Ul Haq, Q. Mahmood, M. S. Al-Buriahi and M. Morsi, First-principles calculations to investigate electronic, structural, optical, and thermoelectric properties of semiconducting double perovskite Ba2YBiO6, *Micro Nanostruct.*, 2022, **170**, 207397.

20 S. Hu, Z. Ren, A. B. Djurišić and A. L. Rogach, Metal Halide Perovskites as Emerging Thermoelectric Materials, *ACS Energy Lett.*, 2021, **6**, 3882–3905.

21 S. A. Khandy, S. Yousuf, T. M. Bhat, S. Singh, S. A. Sofi, S. A. Mir, A. Q. Seh, M. Nabi, N. A. Ganie, A. Rasool, R. A. Mir, P. Kumar and D. C. Gupta, Forecasting electronic-band structure and magnetism in complex double perovskite Ba2CdReO6, *AIP Conf. Proc.*, 2020, **2265**(1), 030359.

22 A. Hanif, S. A. Aldaghfag, A. Aziz, M. Yaseen and A. Murtaza, Theoretical investigation of physical properties of Sr2XNbO6 (X = La, Lu) double perovskite oxides for optoelectronic and thermoelectric applications, *Int. J. Energy Res.*, 2022, **46**(8), 10633–10643.

23 B. Rameshe, M. Rajagopalan and B. Palanivel, Electronic structure, structural phase stability, optical and thermoelectric properties of Sr2AlM'O6 (M'= Nb and Ta) from first principle calculations, *Comput. Condens. Matter*, 2015, **4**, 13–22.

24 S. A. Dar, R. Sharma, V. Srivastava and U. K. Sakalle, Investigation on the electronic structure, optical, elastic, mechanical, thermodynamic and thermoelectric properties of wide band gap semiconductor double perovskite Ba2InTaO6, *RSC Adv.*, 2019, **9**, 9522–9532.

25 S. Al-Qaisi, M. A. Ali, T. A. Alrebdi, T. V. Vu, M. Morsi, B. U. Haq, R. Ahmed, Q. Mahmood and S. A. Tahir, First-principles investigations of Ba2NaIO6 double perovskite semiconductor: material for low-cost energy technologies, *Mater. Chem. Phys.*, 2022, **275**, 125237.

26 S. Al-Qaisi, M. Mushtaq, J. S. Alzahrani, H. Alkhaldi, Z. Alrowaili, H. Rached, B. U. Haq, Q. Mahmood, M. Al-Buriahi and M. Morsi, First-principles calculations to investigate electronic, structural, optical, and thermoelectric properties of semiconducting double perovskite Ba2YBiO6, *Micro Nanostruct.*, 2022, **170**, 207397.

27 S. A. Khandy, S. Yousuf, T. Bhat, S. Singh, S. Sofi, S. Mir, A. Q. Seh, M. Nabi, N. Ganie and A. Rasool, Forecasting electronic-band structure and magnetism in complex double perovskite Ba2CdReO6, *AIP Conf. Proc.*, 2020, 030359.

28 (*a*) A. Hanif, S. A. Aldaghfag, A. Aziz, M. Yaseen and A. Murtaza, Theoretical investigation of physical properties of Sr2XNbO6 (X= La, Lu) double perovskite oxides for optoelectronic and thermoelectric applications, *Int. J. Energy Res.*, 2022, **46**, 10633–10643; (*b*) S. Haid, W. Benstaali, A. Abbad, B. Bouadjemi, S. Bentata and Z. Aziz, Thermoelectric, structural, optoelectronic and magnetic properties of double perovskite Sr2CrTaO6: first principle study, *Mater. Sci. Eng., B*, 2019, **245**, 68–74.

29 J. A. Abraham, D. Behera, K. Kumari, A. Srivastava, R. Sharma and S. K. Mukherjee, A comprehensive DFT analysis on structural, electronic, optical, thermoelectric,

SLME properties of new Double Perovskite Oxide Pb2ScBiO6, *Chem. Phys. Lett.*, 2022, **806**, 139987.

30 M. Manzoor, D. Behera, R. Sharma, F. Tufail, M. W. Iqbal and S. K. Mukherjee, Investigated the structural, optoelectronic, mechanical, and thermoelectric properties of Sr2BTaO6(B=Sb,Bi) for solar applications, *Int. J. Energy Res.*, 2022, **46**, 23698–23714.

31 P. Kazin, A. Abakumov, D. Zaytsev, Y. D. Tretyakov, N. Khasanova, G. Van Tendeloo and M. Jansen, Synthesis and crystal structure of Sr2ScBiO6, *J. Solid State Chem.*, 2001, **162**, 142–147.

32 P. E. Kazin, D. D. Zaitsev, Y. D. Tret'yakov and M. Jansen, Phase Relations in the Bi–(Pb)–Sr–Ca–Cu– Sc–O System, *Inorg. Mater.*, 2001, **37**, 1046–1050.

33 K. Schwarz, P. Blaha and G. K. Madsen, Electronic structure calculations of solids using the WIEN2k package for material sciences, *Comput. Phys. Commun.*, 2002, **147**, 71–76.

34 D. Bowler, Density functional theory: a tale of success in three codes, *J. Phys.: Condens. Matter*, 2016, **28**, 421001.

35 W. Kohn and L. J. Sham, Self-Consistent Equations Including Exchange and Correlation Effects, *Phys. Rev.*, 1965, **140**, A1133.

36 J. P. Perdew, K. Burke and M. Ernzerhof, Generalized gradient approximation made simple, *Phys. Rev. Lett.*, 1996, **77**, 3865.

37 Z. Wu and R. E. Cohen, *Phys. Rev. B: Condens. Matter Mater. Phys.*, 2006, **73**, 235116.

38 J. P. Perdew, A. Ruzsinszky, G. I. Csonka, O. A. Vydrov, G. E. Scuseria, L. A. Constantin, X. Zhou and K. Burke, *Phys. Rev. Lett.*, 2008, **100**, 136406.

39 F. Tran and P. Blaha, Accurate band gaps of semiconductors and insulators with a semilocal exchange-correlation potential, *Phys. Rev. Lett.*, 2009, **102**, 226401.

40 G. K. Madsen and D. J. Singh, BoltzTraP. A code for calculating band-structure dependent quantities, *Comput. Phys. Commun.*, 2006, **175**, 67–71.

41 P. Blaha, K. Schwarz, G. K. Madsen, D. Kvasnicka and J. Luitz, *WIEN2K, An Augmented Plane Wave + Local Orbitals Program for Calculating Crystal Properties*, ed. K. Schwarz, Vienna University of Technology, Austria, 2001.

42 M. Jamal, *Cubic-elastic*, 2014, **https://www.WIEN2k.at/reg_user/unsupported/cubic-elast/(2012)**.

43 F. Birch, Finite Elastic Strain of Cubic Crystals, *Phys. Rev.*, 1947, **71**, 809–824.

44 C. Li, X. Lu, W. Ding, L. Feng, Y. Gao and Z. Guoet, Formability of ABX3 (X = F, Cl, Br, I) halide perovskites, *Acta Crystallogr., Sect. B: Struct. Sci.*, 2008, **64**, 702.

45 S. Pugh, XCII. Relations between the elastic moduli and the plastic properties of polycrystalline pure metals, *London, Edinburgh Dublin Philos. Mag. J. Sci.*, 1954, **45**, 823–843.

46 D. Pettifor, Theoretical predictions of structure and related properties of intermetallics, *Mater. Sci. Technol.*, 1992, **8**, 345–349.

47 O. L. Anderson and H. H. Demarest Jr, Elastic constants of the central force model for cubic structures: polycrystalline aggregates and instabilities, *J. Geophys. Res.*, 1971, **76**, 1349–1369.

48 C. Jasiukiewicz and V. Karpus, Debye temperature of cubic crystals, *Solid State Commun.*, 2003, **128**, 167–169.

49 H. Bendjilali, S. Gheriballah, A. Chahed, *et al.*, Density functional theory investigations of structural, elastic, optoelectronic and thermoelectric properties of the lead-free niobium-based double perovskite oxides (Ba/Sr/Ca)$_2$GaNbO$_6$: materials for optoelectronic devices, *Indian J. Phys.*, 2023, **97**, 4233–4245.

50 R. Chaurasiya, S. Auluck and A. Dixit, Cation modified A2(Ba, Sr and Ca) ZnWO6 cubic double perovskites: a theoretical study, *Comput. Condens. Matter*, 2018, **14**, 27–35.

51 C. Ambrosch-Draxl and J. O. Sofo, Linear optical properties of solids within the full-potential linearized augmented planewave method, *Comput. Phys. Commun.*, 2006, **175**, 1–14.

52 L. Yu and A. Zunger, Identification of potential photovoltaic absorbers based on first-principles spectroscopic screening of materials, *Phys. Rev. Lett.*, 2012, **108**, 68701.

53 M. A. Blanco, E. Francisco and V. Luaña, GIBBS: isothermal-isobaric thermodynamics of solids from energy curves using a quasi-harmonic Debye model, *Comput. Phys. Commun.*, 2004, **158**, 57–72.

54 A. Otero-de-la Roza, D. Abbasi-Pérez and V. Luaña, Gibbs2: a new version of the quasiharmonic model code. II. Models for solid-state thermodynamics, features and implementation, *Comput. Phys. Commun.*, 2011, **182**, 2232–2248.

55 A. Otero-de-la Roza and V. Luaña, Gibbs2: a new version of the quasi-harmonic model code. I. Robust treatment of the static data, *Comput. Phys. Commun.*, 2011, **182**, 1708–1720.

56 Y. Okamato, A. Sakamaki and A. Takeneka, *J. Appl. Phys.*, 2016, **119**, 205106.

57 S.-D. Guo, *et al.*, *New J. Phys.*, 2017, **19**, 113044.

58 Q. Wang, J. Huang, C. Wang, P. Luo, Z. Li, R. Liu, Q. Ma and J. Luo, *ACS Appl. Energy Mater.*, 2021, **4**(11), 12458–12465.

59 G. A. Slack, *J. Phys. Chem. Solids*, 1973, **34**, 321–335.

60 T. Jia, G. Chen and Y. Zhang, *Phys. Rev. B*, 2017, **95**, 155206.

61 K. C. Bhamu, Revealing optoelectronic and transport properties of potential perovskites Cs2PdX6 (X = Cl, Br): a probe from density functional theory (DFT), *Sol. Energy*, 2018, **162**, 336–343.

62 Y. Yin, B. Tudu and A. Tiwari, Recent advances in oxide thermoelectric materials and modules, *Vacuum*, 2017, **146**, 356–374.